Understanding amorphous phase-change materials from the viewpoint of Maxwell rigidity

M. Micoulaut,[1] J.-Y. Raty,[2] C. Otjacques,[2] and C. Bichara[3]

[1]*Laboratoire de Physique Théorique de la Matière Condensée, Université Pierre et Marie Curie, Boite 121, 4 Place Jussieu, 75252 Paris Cedex 05, France*

[2]*Physique de la Matière Condensée, B5, Université de Liège, B4000 Sart-Tilman, Belgium*

[3]*Centre Interdisciplinaire de Nanoscience de Marseille (CINaM), CNRS and Aix-Marseille Universities, Campus de Luminy, Case 913, 13288 Marseille, France*

Phase-change materials (PCMs) are the subject of considerable interest because they have been recognized as potential active layers for nonvolatile memory devices, known as phase-change random access memories. By analyzing first-principles molecular-dynamics simulations we develop a method for the enumeration of mechanical constraints in the amorphous phase and show that the phase diagram of the most popular system (Ge-Sb-Te) can be split into two compositional regions having a well-defined mechanical character: a tellurium rich flexible phase and a stressed rigid phase that encompasses the known PCMs. This sound atomic scale insight should open new avenues for the understanding of PCMs and other complex amorphous materials from the viewpoint of rigidity.

I. INTRODUCTION

Driven by applications in data storage (rewritable DVDs and nonvolatile memories)[1–3] fundamental and applied studies of tellurides using groups III, IV, and V elements are rapidly developing. The most studied phase-change materials (PCMs) belong to the ternary Ge-Sb-Te system with particular compositions such as $Ge_2Sb_2Te_5$ (Ref. 4) used at present in industrial data storage applications.[5] These alloys can sustain a large number of transformation cycles produced either by laser-light pulses or electrical current that allow for a fast switching between a crystalline and an amorphous phase with a high contrast in resistivity or optical reflectivity. A key issue in this context is the understanding of the underlying changes in the atomic structure. This has led to a series of investigations of the structure of both amorphous and crystalline phases using experimental as well as computer simulation techniques (for a review, see Ref. 3). It has been suggested that the origin of the contrast lies in the local environment of the germanium atoms that switch from an octahedral environment in the crystalline state,[6] with six neighbors and bond angles around 90°, to a tetrahedral one with four neighbors and angles around 109°. Support to this model has been given by numerical simulations on crystalline structures.[7] This focus on the contrast has somehow overshadowed the study of other intrinsic properties of the amorphous phase and of their consequences on the practical use of PCMs. Here, we investigate the mechanical properties of a class of amorphous alloys ($Ge_xSb_yTe_{1-x-y}$), and show that PCMs are characterized by common specific features in terms of the network rigidity and topology given by bonding characteristics.

By contrast with lighter chalcogenides for which the so called octet or "8-N" rule (N is the number of s and p electrons) results from the ionocovalent nature of the bonding, its applicability to the heavier and less ionic tellurides is certainly challenging. In parent systems where the 8-N rule holds, particularly sulfur and selenium-based amorphous net-

works, rigidity theory offers a practical computational scheme using topology, namely, the Maxwell counting procedure, and has been central to many contemporary investigations on noncrystalline solids.[8–13] It has led to the recognition of a rigidity transition,[11] which separates flexible glasses, having internal degrees of freedom that allow for local deformations, from stressed rigid glasses which are "locked" by their high bond connectivity. Mathematically, this transition is reached when the number of mechanical constraints per atom n_c equals the number of degrees of freedom, which is three in three dimensions.

What happens if these elements are replaced by heavier elements such as tellurium which would lead to more complicated local structures, as highlighted both from experiments[6,14] and simulations?[15–18] Does the counting procedure still hold? Attempts in this direction have been made on a heuristic basis[19] but they seem to contrast with experimental findings and observations. A firm ground for the Maxwell constraint counting is therefore very much desirable: this is the purpose of the present study which develops a precise enumeration algorithm for constraints arising from bond-stretching (BS) and bond-bending (BB) interactions, based on the analysis of atomic scale trajectories from first-principles molecular-dynamics simulations (FPMD). Combined with rigidity theory, this opens an interesting perspective to study amorphous phase-change materials in much the same fashion as network glasses.

As a result, we show that the phase diagram of the Ge-Sb-Te system can be separated into two compositional regions having a well-defined mechanical character derived from rigidity theory: a flexible Te-rich phase and a (Sb,Ge)-rich phase that is stressed rigid. The most commonly used Ge-Sb-Te (GST) phase-change materials belong to this second category. While this result may be considered as trivial since underconstrained Te alloyed with cross-linking overconstrained elements (Ge,Sb) will inevitably lead to two phases, flexible and stressed rigid, it proves to be highly complex and nontrivial. In fact, the location of the rigidity transition line and the constraint map are found to be sub-

stantially modified with respect to isochemical compounds (e.g., Ge-As-Se) for which the 8-*N* rule holds.

The paper is organized as follows: in Sec. II, we describe the method introduced, i.e., how trajectories from first-principles molecular-dynamics simulations can be used to investigate the neighborhood of a given atom and how the angular motion can be split in relevant and nonrelevant contributions to bonding constraints. We first apply the method to the benchmark system $GeSe_2$ for which the direct Maxwell constraint counting is straightforward. In Sec. III, we move to amorphous GST materials and compute for seven selected compositions in the Ge-Sb-Te system bond-stretching and bond-bending constraints. Having in hand the latter, we show in Sec. IV that a rigidity transition can be found. Finally, Sec. V summarizes our results and some perspectives are drawn.

II. FROM TRAJECTORIES TO BONDING CONSTRAINTS

A. Simulation details

The calculations on benchmark system $GeSe_2$ (see results below) were performed at constant volume on a system consisting of 40 germanium and 80 selenium atoms. A periodically repeated cubic cell of size 15.7 Å was used to match the measured experimental density.[20] The system was first relaxed for 20 ps at 1373 K and then 60 ps at 1050 K (see Ref. 21) prior to a quench at room temperature (300 K). The electronic structure was calculated within a density-functional theory (DFT) approximation coupled to a Car-Parrinello algorithm for the ionic motion.[22] The exchange-correlation functional Becke, Lee, Yang and Parr (BLYP)[23] in a general gradient approximation (GGA) was used, and valence electrons have been treated explicitly to account for core-valence interactions. The wave functions have been expanded at the Γ point of the supercell on a plane-wave basis set defined by an energy cutoff $E_c=20$ Ry. We used a fictitious electron mass of $\mu=600$ a.u. (in units of $m_e a_0^2$, where m_e is the electronic mass and a_0 is the Bohr radius) and a time step of $t=0.1$ fs to integrate the equations of motion. Temperature control is implemented for both ionic and electronic degrees of freedom by using Nosé-Hoover thermostats.[24] The amorphous phase was obtained by quenching the 1050 K down to 300 K by steps of 100 K with at least 2 ps equilibration at each step. Statistics in the amorphous state were finally accumulated over a set of 30 ps.

The seven compounds of the GST triangle have been simulated using the VASP software package[25] using projector augmented wave (PAW) potentials[26] for GeTe and ultrasoft pseudopotentials[27] for the other compounds together with the Perdew-Wang (PW91) GGA.[28] The electronic structure was computed within DFT and expanded on a plane wave basis. The energy cutoff for the plane-wave expansion was 10.56 Ry (Sb_2Te_3 and Sb_2Te), 12.79 Ry ($GeSb_6$, $Ge_1Sb_2Te_4$, and $Ge_2Sb_2Te_5$), and 18.38 Ry (GeTe and $GeTe_6$). Such a large cutoff was needed to reproduce the fine details of the amorphous structures, as it was the case for crystalline GeTe.[29] This is due to the extremely flat potential valley around the minimum (distorted) energy structure. The amorphous structures were generated using Born-Oppenheimer molecular dy-

namics at the Γ point with a 3 fs integration time step. The temperature was controlled through a Nosé thermostat[24] with a 3 a.u. fictitious mass. The atoms (125 for Sb_2Te_3, 178 for $Ge_1Sb_2Te_4$, 162 for $Ge_2Sb_2Te_5$, 210 atoms for Sb_2Te and GeTe, and 216 for $GeSb_6$ and $GeTe_6$, respectively) were initially set in a NaCl arrangement at the experimental amorphous density. The system was then heated for more than 10 ps at 3000 K, followed by 10–20 ps equilibration at the experimental melting temperature. It was then quenched down to 100 K in 50 K steps, with at least 2 ps equilibration at each step. This total quench time of 20–60 ps is significantly faster than the real quench and this essentially results in the limited possibility to alter the chemical order by atomic diffusion during the quench. Our simulations thus rely on the assumption that the chemical order is similar in both amorphous and liquid phases.

B. Estimate of constraints: General setting

At the heart of the rigidity concept is the identification of relevant interatomic forces between atoms in a manner similar to what Maxwell pioneered for trusses and macroscopic structures.[30] In mechanical engineering, the stability of such structures depends on the balance between forces acting on the node of a truss (i.e., the number of bar tensions connecting the node that is the number of Lagrangian constraints[31]) and its number of degrees of freedom. When applied to covalent amorphous networks and once the forces acting as constraints are identified (BS and BB forces), a similar analysis can be performed leading to the Phillips-Thorpe rigidity transition,[11] which separates flexible (underconstrained) networks from stressed rigid (overconstrained) networks.[8–13] At the transition, a vanishing of the number of low-frequency modes (floppy modes) f is obtained,[11] where f represents internal degrees of freedom which permit local deformations of the network.

As in standard mechanics, however, instead of treating forces and querying about motion, one can ask the opposite question and try to relate motion to the absence of a restoring force. This is done in the present approach from FPMD. We generate atomic scale trajectories of various amorphous systems at low temperature using the aforementioned electronic models and apply a structural analysis in relation with rigidity theory. The statistical analysis is performed by averaging over space (structure average) and time (trajectories).

1. Neighbor distributions

Since we are dealing with octahedral and possibly tetrahedral structures, around each atom in a given structure, we consider at least the six first neighbors i that are sorted according to their distance and we analyze the distribution $h_i(r)$ of these distances, as first done in Ref. 15, the sum of which yields the pair correlation function $g(r)$. The actual number of neighbors r, and hence the number of BS constraints, is calculated here by integrating the radial distribution function up to its first minimum. According to the constraint enumeration, one has $r/2$ BS constraints for a r-coordinated atom.[11]

2. Partial bond angle distributions

To estimate the number of bond-bending constraints we analyze partial bond angle distributions (PBADs) defined as
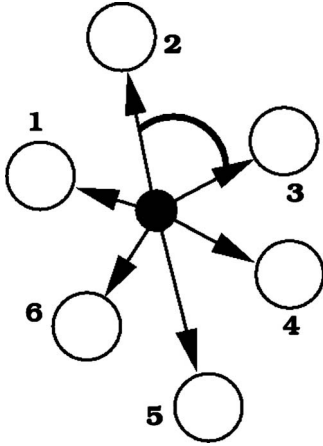
FIG. 1. A schematic picture for the calculation of partial bond angle distributions (PBADs): N closest neighbors (open circles) are selected around a central atom 0 (filled circle), which define corresponding angles (the marked one corresponds to angle 203). The angle number assignment can be found in Figs. 3 and 9. See text for details

follows. For each type of central atom 0, the six first neighbors i are selected and sorted according to their distances and the PBADs $P(\theta_{ij})$ of the 15 corresponding angles $i0j$ ($i=1,\ldots,5$, $j=2,\ldots,6$) are calculated, i.e., 102, 103, 203, etc. (Fig. 1). The choice of looking up to $j=6$ is motivated by the fact that in telluride systems octahedral local structures with six neighbors around a central atom are expected in both the crystalline[6] and amorphous phases.[18] Reduction to a lower number of possible neighbor or angles in, e.g., the case of purely tetrahedral systems, is straightforward, as noticed below from the angle number assignment.

The standard deviation $\sigma_{\theta_{ij}}$ of $P(\theta_{ij})$ (or full width at half maximum in case of a regular distribution) provides a quantitative estimate of the angular excursion around the mean value $\overline{\theta}_{ij}$ of angle $i0j$, thus measuring the strength of the bond-bending restoring force. An angle displaying a wide $\sigma_{\theta_{ij}}$ corresponds to a broken BB constraint as there is a weak interaction to maintain the angle fixed. In an opposite way, sharp bond angle distributions lead to intact constraints. This way of analyzing the results of FPMD simulations provides a firm basis for the enumeration of BS and BB constraints in complex materials.

We have also checked for system size effects for selected compositions. Of course, realistically probing the effect of system size on the neighbor distributions and PBAD's would require a significant change in the box sizes, on all seven alloy compositions studied, certainly beyond the standard computational capabilities. We already used large boxes, up to $\simeq 200$ atoms, which are comparable to other studies in the field.[16,17] One can reasonably estimate that if the pair correlation is correct up to a distance equal to half of the smallest cell dimension (in the present case, this is approximately equal to 8 Å), the angular distribution between first neighbors (bonds smaller than typically 3.2 Å) angle are also very well converged. As a test, we have compared the partial pair distribution functions (PDFs) and PBADs of the Sb_2Te_3 system, which has been simulated with the same thermal history
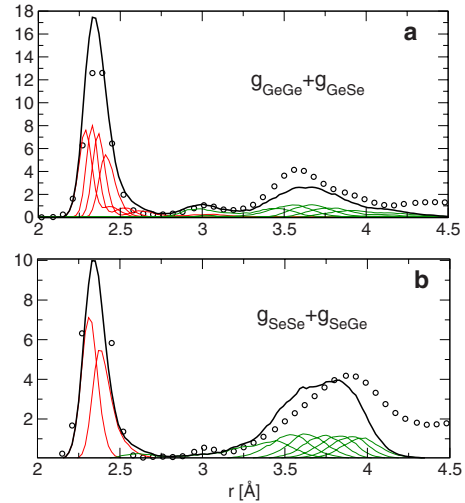

FIG. 2. (Color online) (a) Experimental Ge-centered pair distribution function $g_{GeGe}+g_{GeSe}$ [circles, data from Petri *et al.* (Ref. 32)] together with the distribution of neighbors (first four neighbors in red, others in green) and the total contribution of neighbors (black solid line). (b) Experimental Se-centered pair distribution function $g_{SeGe}+g_{SeSe}$ (circles) together with the distribution of neighbors (first two neighbors in red, others in green) and the total contribution of neighbors (solid line).

using two different box sizes (125 and 210 atoms). Agreement between the PDF's obtained with the different box sizes is quasiperfect, and while PBAD's have small differences in shape, the extracted second moment (standard deviations) of the distributions are nearly identical.

C. Benchmark case GeSe$_2$

In order to check this method, we first apply it to the benchmark case GeSe$_2$, for which application of constraint counting algorithms is straightforward.[11] According to the Phillips-Thorpe enumeration, one has for a r-coordinated atom, respectively, $r/2$ and $2r-3$ BS and BB constraints. Thus a fourfold Ge atom has two BS and five BB constraints whereas the twofold selenium atom has one BS and one BB constraint leading to an overall number of constraints per atom, n_c, equal to 3.67.[11]

We have computed the Ge- and Se-centered pair distribution functions and the neighbor distributions (Fig. 2). These pair distribution functions reproduce very well the experimental data from Salmon and co-workers.[32] At short distances, and up to $r=3.5-4$ Å, the sum of all neighbors distributions also agree well with experiments. It can be clearly seen from Fig. 2(a) that Ge has $r=4$ neighbors contributing to the first peak, well separated from the other neighbors (which leads to the minimum observed in $g_{GeSe}+g_{GeGe}$ around 2.75 Å). Integration of the first peak up to the minimum at 2.75 Å (respectively, 2.78 Å for selenium) leads to similar values (respectively, 4.01 and 1.97 for Ge and Se). Since the number of BS constraints is equal to $r/2$, it leads to a respective number of BS constraints of two and one for Ge and Se atoms.

We furthermore find that $\sigma_{\theta_{ij}}$ can vary between 10° and 40° depending on the different angles $i0j$ considered (Fig. 3).
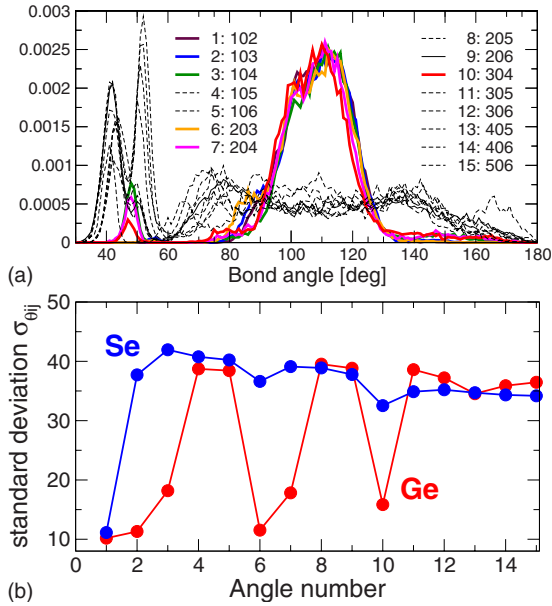
FIG. 3. (Color online) (a) Ge-centered partial bond angle bond angle distributions (PBADs, up to 15) for various triplets of atoms $i0j$ ($i=1,\ldots,6$, $j=2,\ldots,5$) in amorphous GeSe$_2$. The six colored distributions have a low standard deviation [typically $10°-20°$, see panel (b)]. The angle number assignments ($1,\ldots,15$) displayed in the Ge panel are valid for all other angular studies. (b) Standard deviation $\sigma_{\theta_{ij}}$ of the distributions as a function of the angle number in amorphous GeSe$_2$: Ge- (red) and Se- (blue) centered angles.

For the Ge-centered atoms, six standard deviations $\sigma_{\theta_{ij}}$ are found to be on the order of $10°-15°$, clearly separated by a gap of about $20°$ from all others for which $\sigma_{\theta_{ij}} \simeq 40°$. However, there is one redundant constraint that needs to be removed because it can be determined from the five other angles. This leaves the estimate with five independent BB constraints for the Ge atom. For the Se atom, a single low $\sigma_{\theta_{ij}}$ (i.e., a single BB constraint) is found ($12°$) around the mean value $\bar{\theta}_{ij}=100°$, in agreement with experiment.[33] We thus show that the constraint computation from FPMD matches exactly the direct counting from Ref. [11].

III. AMORPHOUS GE-SB-TE MATERIALS

A. Structural results

As shown in Fig. 4 for amorphous GeTe and Ge$_2$Sb$_2$Te$_5$ the structure factors obtained from the simulations compare favorably with the available experimental $S(q)$ obtained by x-ray scattering.[34] All peaks (and especially the first ones found around 2, 3.2, and 5 Å^{-1}) are reasonably well reproduced in height and position.

Turning to real space properties, we first stress that our amorphous Ge$_2$Sb$_2$Te$_5$ structure is very close to that obtained separately by Akola and Jones,[16] and by Caravati *et al.*,[17] which use the same DFT scheme and a similar simulation box size. Our results differ slightly from those obtained in an elongated cell, in which the smallest dimension is only on the order of three to four interatomic bonds.[35] It suggests that the shape of the simulation box may affect results on coor-
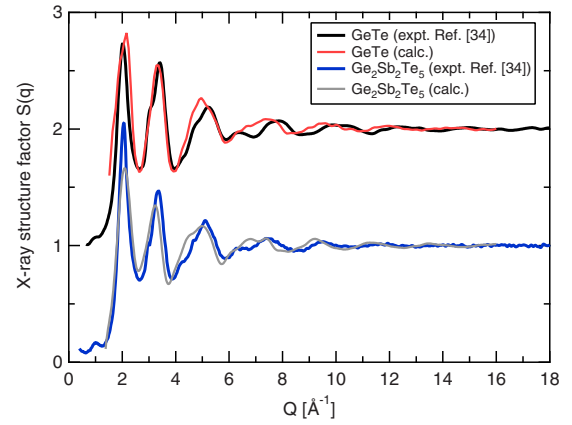

FIG. 4. (Color online) Comparison between our model amorphous $S(q)$ of GeTe (101) and Ge$_2$Sb$_2$Te$_5$ (225) and the experimental x-ray $S(q)$ data (Ref. [34]).

dination numbers. However, we have checked that the present results were robust in terms of size effects by comparing simulations on cubic boxes with 125 and 210 atoms. The Ge-Te and Sb-Te distances are, respectively, found at 2.78 and 2.93 Å, close to experimental findings from x-ray diffraction and extended x-ray absorption fine structure (EXAFS).[6,36] A full structural analysis of the seven alloys investigated is not the purpose of this paper, and will be given elsewhere.

In order to avoid a cumbersome presentation, we focus on the most interesting histograms $h_i(r)$ ($i=1,\ldots,6$) of the six first neighbors contributions around selected atomic species calculated from the trajectories obtained by FPMD on Ge-Sb-Te alloys in the amorphous phase. They are presented in Figs. 5–7. Noteworthy at a first glance is the fact that the Ge environment is very different in these materials, when compared to GeSe$_2$, as emphasized by the absence of a clear gap between the first and second shells of neighbors [2.75 Å in GeSe$_2$, see Fig. 2(a)]. Furthermore, GeTe$_6$ (106), Ge$_1$Sb$_2$Te$_4$ (124), and Ge$_2$Sb$_2$Te$_5$ (225) display a bimodal distribution for the fourth neighbor distribution (Fig. 5) around Ge atoms. These two contributions arise from the mixture of (distorted) octahedral and tetrahedral environments (see Ref. [37] for a detailed analysis). A closer examination of the structure allows the determination of the fraction η_4 of tetrahedral Ge species used below.

The present findings contrast with those found in absence of tellurium as in GeSb$_6$, shown in Fig. 6: around Ge atoms, a clear separation is found between the first four equivalent neighbors and the remaining fifth and sixth neighbors. These features are indicative of a tetrahedral environment also evidenced by the angular analysis (see below).

In systems without germanium, e.g., Sb$_2$Te (Fig. 7), an intermediate fourth neighboring atom can be found between the first shell ($i=1,\ldots,3$) and the second shell of neighbors ($i=5,6$) around a central Sb atom. Similarly, the coordination number of Te is here obviously larger than two, as $h_3(r)$ will be found close to the location of the minimum of the Te-centered pair distribution function.

By integrating the properly weighted partial radial distribution functions, the number of neighbors $n_i(r)$ around each
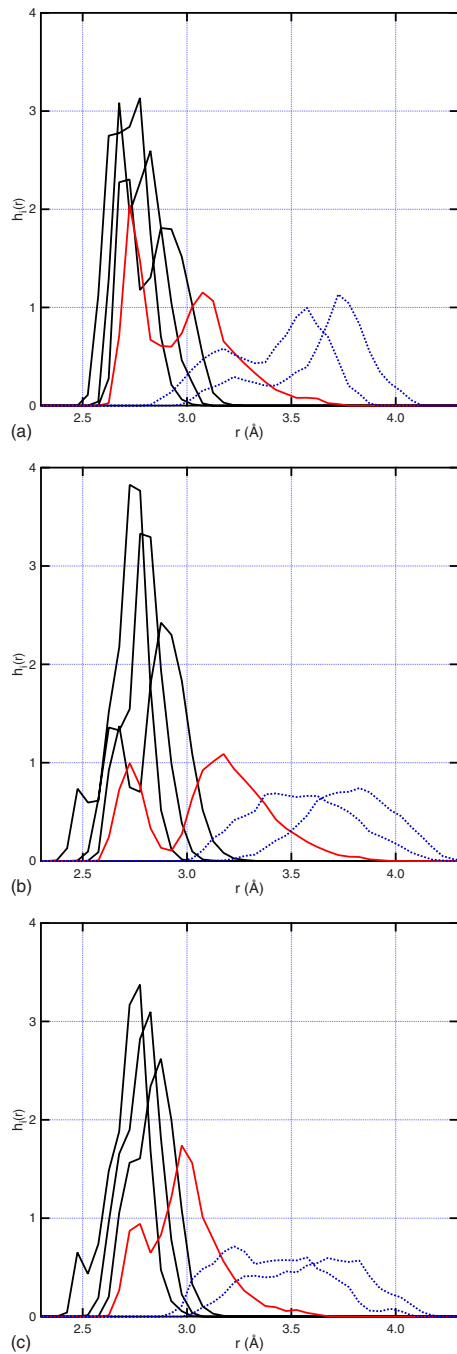
(a)

(b)

(c)

FIG. 5. (Color online) Histograms $h_i(r)$ of the six first neighbors contributions around Ge species in amorphous GeTe$_6$ (101, top), Ge$_1$Sb$_2$Te$_4$ (124), and Ge$_2$Sb$_2$Te$_5$ (225, bottom) alloys. Full black lines correspond to the short bonds contributing to the first peak in pair distribution functions (PDFs), while dashed blue lines correspond to neighbors lying beyond the first minimum of the PDF (second neighbor shell). Red lines correspond to the fourth neighbor distribution, spanning these two shells. The bimodal character of the first shell indicates that distorted octahedral and tetrahedral environments for Ge atoms coexist.

atomic species as a function of the integration distance can be obtained. This allows us to extract a coordination number r_i (i=Ge,Sb,Te) to be used as input for the count of BS
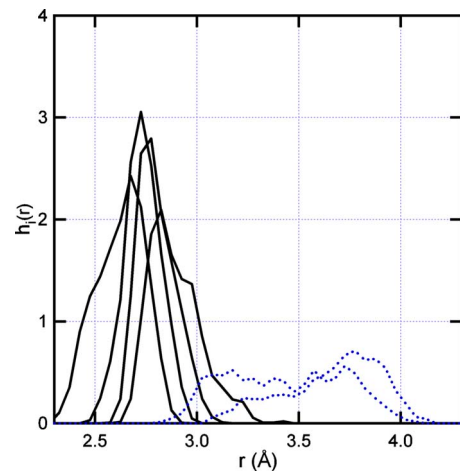

FIG. 6. (Color online) Histograms $h_i(r)$ of the six first neighbors contributions around Ge species in amorphous GeSb$_6$ (160). Black curves are assigned to the first four neighbors, while dotted blue curves are assigned to neighbors 5 and 6.

constraints. Figure 8 shows this quantity $n_i(r)$ as a function of the radial distance. We used the most commonly accepted
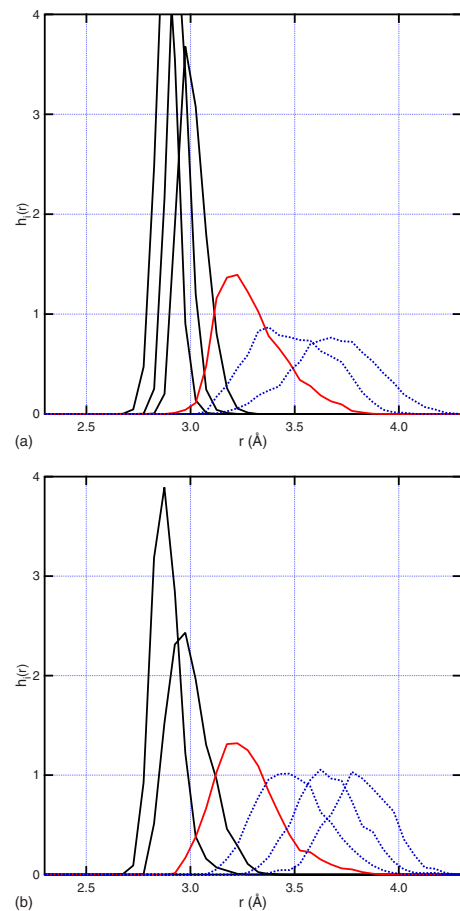

(a)

(b)

FIG. 7. (Color online) Histograms $h_i(r)$ of the six first neighbors contributions around Sb (top) and Te (bottom) species in amorphous Sb$_2$Te (021). Black curves are assigned to the first neighbors, red curves to the neighbor distribution located at the g(r) minimum, while dotted blue curves are assigned to neighbors 5 and 6.
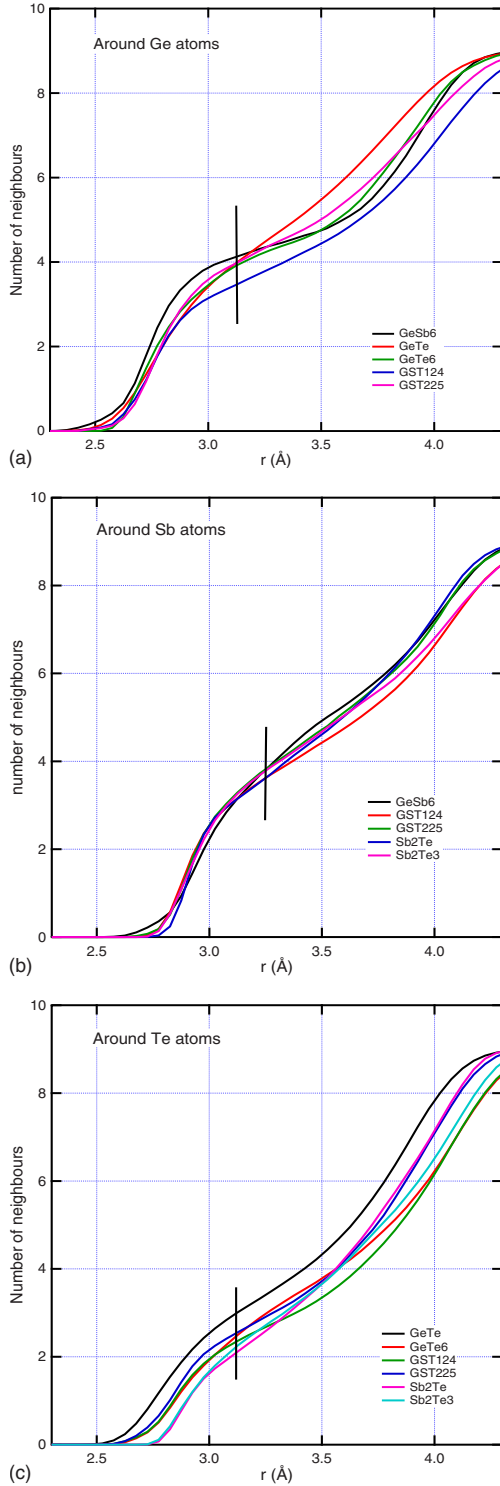
FIG. 8. (Color online) Integrated number of neighbors $n_i(r)$ around Ge, Sb, and Te atomic species in selected amorphous Ge-Sb-Te systems. The vertical bar indicates the distance cutoff chosen to calculate the number of first neighbors r_i, and hence the BS constraints.

rule by integrating the radial distribution function up to its first minimum and we checked the influence of reasonable changes in the location of this minimum. The maximum error on the number of neighbors is ± 0.3, and half of it on the

TABLE I. Coordination number r_i of the atomic species, giving the number of BS constraints ($r_i/2$), number of BB constraints n_i^{BB} computed from the standard deviations of the PBADs $P(\theta_{ij})$, and total number of constraints n_c in the seven different Ge-Sb-Te compounds. Cutoff distances to calculate r_i are 3.17, 3.22, and 3.17 Å for Ge, Sb, and Te, respectively. Error bars on r_i are calculated using cutoff values of ± 0.08 Å. BB constraints, corresponding to a number of rigid angles, are integer values for Sb and Te. Since Ge may display two different environments, with three BB constraints for distorted octahedral, and five for tetrahedral, a weighted average is taken, with error bars arising from the tetrahedral fraction (η_4) estimate. See text for details.

Compound	Atom	r_i	n_i^{BB}	n_c
GeTe$_6$	Ge	4.0 ± 0.2	3.3 ± 0.1	2.73 ± 0.16
	Te	2.6 ± 0.3	1.0	
GeTe	Ge	4.2 ± 0.3	3.1 ± 0.1	3.87 ± 0.17
	Te	3.1 ± 0.2	1.0	
Ge$_1$Sb$_2$Te$_4$	Ge	3.7 ± 0.3	3.4 ± 0.1	3.42 ± 0.14
	Sb	3.7 ± 0.3	3.0	
	Te	2.5 ± 0.2	1.0	
Ge$_2$Sb$_2$Te$_5$	Ge	4.1 ± 0.2	3.2 ± 0.1	3.57 ± 0.12
	Sb	3.9 ± 0.2	3.0	
	Te	2.7 ± 0.2	1.0	
GeSb$_6$	Ge	4.2 ± 0.1	5.0	5.26 ± 0.14
	Sb	3.9 ± 0.3	3.0	
Sb$_2$Te	Sb	3.8 ± 0.2	3.0	4.00 ± 0.10
	Te	2.4 ± 0.2	1.0	
Sb$_2$Te$_3$	Sb	3.7 ± 0.3	3.0	3.23 ± 0.12
	Te	2.3 ± 0.2	1.0	

BS contribution to the constraint. For additional check, we quenched the liquid configurations of the Ge$_1$Sb$_2$Te$_4$ alloy, obtained at three densities[18] and checked that the corresponding changes in number of neighbors remained within these error bars.

B. Stretching and bending constraints

Having shown that this method was able to reproduce the Maxwell constraint count for GeSe$_2$, we now turn to the amorphous Ge-Sb-Te system and focus on the constraint analysis of the seven particular compositions, namely, Ge$_1$Sb$_2$Te$_4$ (124), Ge$_2$Sb$_2$Te$_5$ (225), GeTe (101), GeTe$_6$ (106), GeSb$_6$ (160), Sb$_2$Te (021), and Sb$_2$Te$_3$ (023) (see also Fig. 14). We determine (Table I) the BS constraints from the coordination numbers extracted from Fig. 8. The coordination number of Ge and Sb is nearly equal to $r=4$, with a preference for heteropolar bonding with Te atoms, which have a coordination number between 2.1 and 2.9, larger than the 8-N value ($r=2$) as seen from the particular example of Sb$_2$Te (Fig. 7).

The Ge-, Sb-, and Te-centered PBADs $P(\theta_{ij})$ for the 124 compound are displayed in Fig. 9. Some specific angles clearly display a limited motion around their mean value $\bar{\theta}_{ij}$. Figures 10–12 show the 15 different mean angles (first mo-
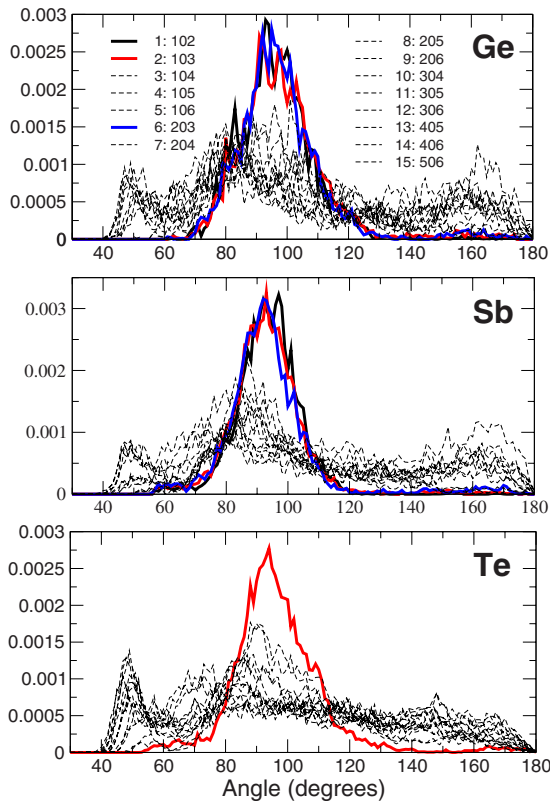
FIG. 9. (Color online) Ge-, Sb-, and Te-centered bond angle distribution in the $Ge_1Sb_2Te_4$ (124) amorphous system. The curves in color correspond to distributions with a low standard deviation $\sigma_{\theta_{ij}}$ considered as having intact BB constraints. The peaks around $50°$ correspond to the steric hindrance (hard-core repulsion between neighboring atoms).

FIG. 10. (Color online) Mean angle $\bar{\theta}_{ij}$ and angular standard deviation $\sigma_{\theta_{ij}}$ of the PBADs of $Ge_1Sb_2Te_4$ (124) amorphous systems as a function of angle number for Ge- (black), Sb- (red), and Te- (blue) centered atoms. The correspondence between angle number (x axis) and angles ($i0j$), with 0 as the central atom and i and j as the neighbors, is given in Figs. 3 and 9. Only three Ge and Sb (one Te) angles have a low $\sigma_{\theta_{ij}}$, corresponding to intact BB constraints.

C. Discussion

The present results contrast with the view that would follow the standard enumeration of constraints, directly derived from coordination numbers obeying the 8-N rule. In fact, a threefold Sb would give rise to 1.5 BS and 3 BB constraints.[11] Here, Sb has an additional neighbor that increases the number of BS constraints to 2, but it does not give rise to two additional BB constraints (Figs. 10 and 11).

ments) $\bar{\theta}_{ij}$ and the standard deviations $\sigma_{\theta_{ij}}$ for the compositions 124, 225, and 160, leading to the determination of corresponding BB constraints for Ge, Sb and Te atoms. Compared to the benchmark system $GeSe_2$, we notice that $\sigma_{\theta_{ij}}$ is more scattered for large angle number n (i.e., $n > 6$), which suggests an increased orientational disorder when more distant neighbors are considered.

In the ternary compositions 124 and 225, only three standard deviations are on the order of $\sigma_{\theta_{ij}} \simeq 10° - 15°$ for the Ge and Sb atoms, associated with well-defined angles at $\bar{\theta}_{ij} = 90° - 100°$, which define the equatorial plane of the octahedra and are reminiscent of the distorted octahedral-like rocksalt cubic phase.[6,7] All Te-containing systems display a clear splitting between low $\sigma_{\theta_{ij}}$ for intact bond angle constraints and larger standard deviations ($\sigma_{\theta_{ij}} = 30° - 40°$). Those are the cleanest situations when the separation between low and high standard deviations have a significant gap (typically $\Delta\sigma_{\theta_{ij}} = 10° - 15°$). However, with an increased number of constraints (as highlighted by the $GeSb_6$ system of Fig. 12 for which $n_c = 5.26$), this gap tends to decrease because the very large network connectedness now strengthen weaker forces (e.g., torsional forces) and reduce possible second-neighbor motions.
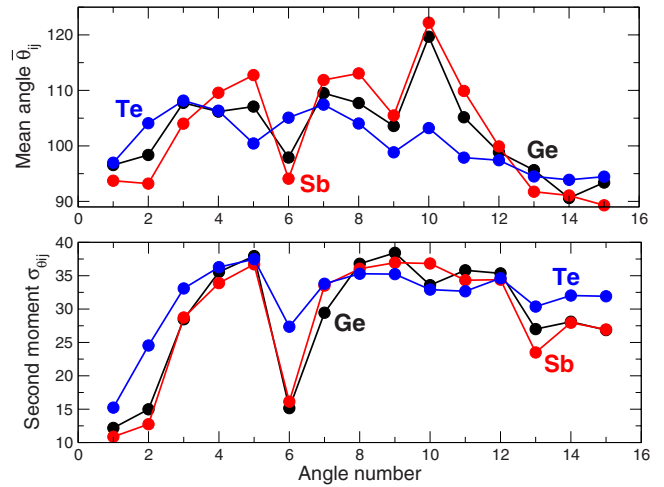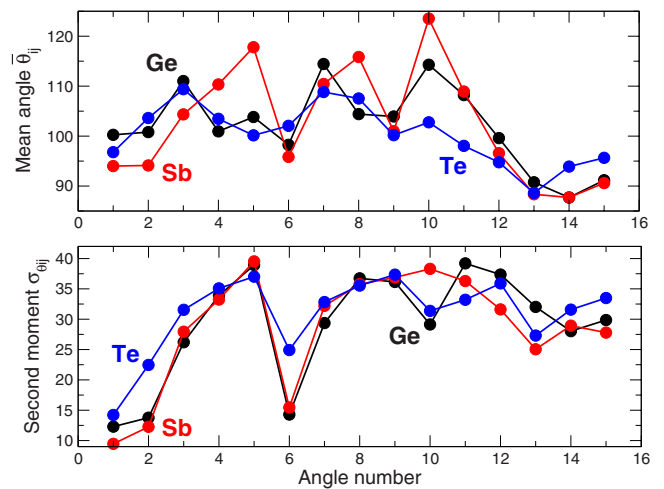

FIG. 11. (Color online) Mean angle $\bar{\theta}_{ij}$ and angular standard deviation $\sigma_{\theta_{ij}}$ of the PBADs of $Ge_2Sb_2Te_5$ (225) amorphous systems as a function of angle number for Ge- (black), Sb- (red), and Te- (blue) centered atoms. The correspondence between angle number (x axis) and angles ($i0j$), with 0 as the central atom and i and j as the neighbors, is given in Figs. 3 and 9. Only three Ge and Sb (one Te) angles have a low $\sigma_{\theta_{ij}}$, corresponding to intact BB constraints.
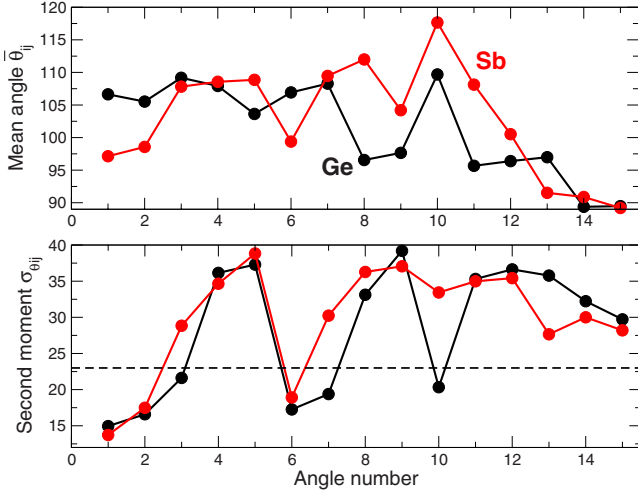
FIG. 12. (Color online) Mean angle $\bar{\theta}_{ij}$ and angular standard deviation $\sigma_{\theta_{ij}}$ of the PBADs of GeSb$_6$ (160) amorphous systems as a function of angle number for Ge- (black) and Sb- (red) centered atoms. The correspondence between angle number (x axis) and angles ($i0j$), with 0 as the central atom and i and j as the neighbors, is given in Figs. 3 and 9.

In 124 and 225, only three Sb angles have a standard deviation of $10° - 15°$ corresponding to mean angles $\bar{\theta}_{ij} = 95°$.

Although tellurium has more than two neighbors ($r_{Te} > 2$), as shown in Fig. 7 for alloy 021, it has only one angular constraint (Fig. 10, $\sigma_{\theta_{ij}} = 12°$ in the 124 and $\bar{\theta}_{ij} \simeq 95°$, also seen from Fig. 9), the two other possible angles (angle number 2: 103 and 6: 203) being much more flexible ($\sigma_{\theta ij} = 27°$ and 29°). On the basis of this enumeration, and using results of Table I and of Figs. 10–12, a Maxwell estimate for the number of BS and BB constraints of Ge$_x$Sb$_y$Te$_{1-x-y}$ is given by

$$n_c = \frac{1}{2}[x(r_{Ge} - r_{Te}) + y(r_{Sb} - r_{Te}) + r_{Te}]$$
$$+ [x(n_{Ge}^{BB} - n_{Te}^{BB}) + y(n_{Sb}^{BB} - n_{Te}^{BB}) + n_{Te}^{BB}], \qquad (1)$$

where the square brackets are used to separate BS from BB contributions. Results for n_c from Eq. (1) are given in Table I.

In order to obtain a counting that takes into account different local topologies, a more subtle analysis is needed to compute the number of constraints in the ternary alloys involving both germanium and tellurium atoms. In fact, two local environments can be found for fourfold Ge in the presence of tellurium as emphasized by Fig. 5: a majority of distorted octahedral sites having three constraints for the angles $\bar{\theta}_{ij} = 90° - 100°$ (see average result in Figs. 10 and 11), and a minority (with fraction η_4) of tetrahedral Ge (calculated to be, respectively, $\eta_4 = 0.1$ and $\eta_4 = 0.2$ in the 225 and 124, also found in Refs. 16 and 17), which have 5 BB constraints as in GeSe$_2$. The determination of BB constraints can be generalized to mixed environments without any ambiguity as seen for Ge$_1$Sb$_2$Te$_4$ (Fig. 13). For instance, after the identification of tetrahedra in Ge$_1$Sb$_2$Te$_4$, it is possible to obtain
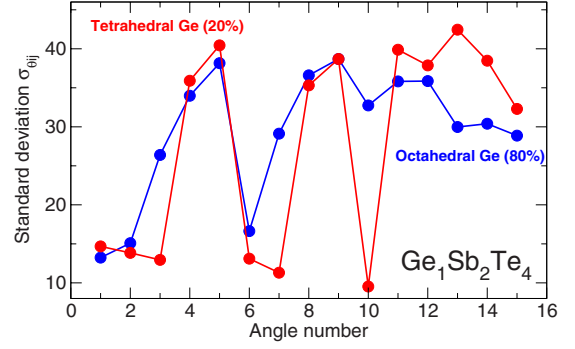

FIG. 13. (Color online) Standard deviation $\sigma_{\theta_{ij}}$ of Ge-centered PBADs for tetrahedral (red) and octahedral (blue) sites in amorphous Ge$_1$Sb$_2$Te$_4$.

the standard deviation $\sigma_{\theta_{ij}}$ depending on the local structure, tetrahedral or octahedral. It appears clearly (Fig. 13) that the tetrahedral Ge sites have six rigid angles, corresponding to five BB constraints as in the GeSe$_2$ benchmark, while the distorted octahedral ones have only three rigid angles and BB constraints. This means that the average number of germanium BB constraints is $n_{Ge}^{BB} = 5\eta_4 + 3(1 - \eta_4) = 3 + 2\eta_4$ and gives for the Maxwell estimate,

$$n_c = \left[r_{Ge}\frac{x}{2} + r_{Sb}\frac{y}{2} + (1 - x - y)r_{Te}\frac{1}{2} \right]$$
$$+ x(3 + 2\eta_4) + 3y + (1 - x - y) \qquad (2)$$

and finally to $n_c^{124} = 3.42$ and $n_c^{225} = 3.57$, with r_{Te} being calculated for each composition using Table I. One can thus conclude that 124 and 225 are stressed rigid, i.e., they have more constraints than degrees of freedom (three in three dimensions). The present results contrast with a constraint enumeration based on EXAFS measurements, and with the reported assumption that GST materials are perfect glasses,[19] but they agree with the obvious observation that, apart the 106 alloy,[38] which is found flexible, but close to the optimal $n_c = 3$, none of the alloys studied can form bulk glasses.

Again, we note that the GeSb$_6$ compound behaves very differently from tellurium containing alloys, as already emphasized in Fig. 6. Integration of the first peak of the pair distribution functions $g_{GeGe} + g_{GeSb}$ and $g_{SbSb} + g_{SbGe}$ leads to a coordination number for Ge and Sb which is, respectively, 4.15 and 3.70. However, the origin of a nearly similar coordination number for both species is quite different. One has indeed an octahedral distorted structure for the Sb atom as manifested by three angles close to a mean angle of 95° (Fig. 12), whereas the closest angles for the Ge atom are indicative of a tetrahedral environment (109°). Corresponding constraints are intact, i.e., they show a low standard deviation, on the order of $15° - 20°$. In this respect, it appears that from the viewpoint of rigidity Sb is close to what is obtained in ternary telluride compounds while Ge is tetrahedral and behaves similarly to what is obtained for GeSe$_2$.

IV. RIGIDITY TRANSITION IN TELLURIDES

Using these elements, we now determine an approximate flexible to rigid transition composition[11] from the Maxwell
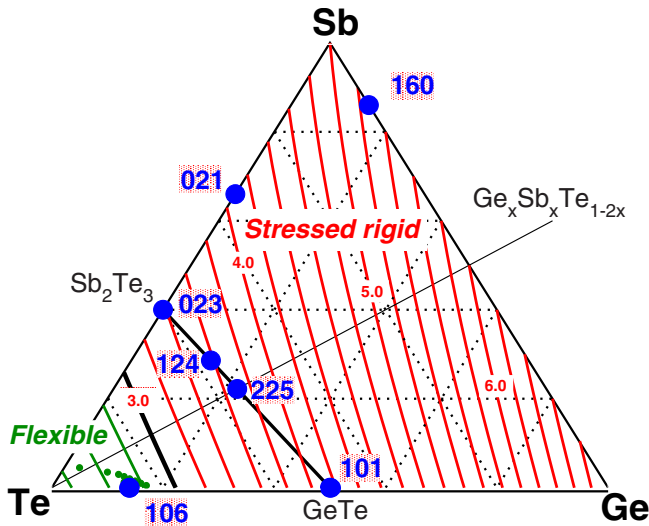
FIG. 14. (Color online) Contour map of the number of constraints n_c in the ternary $Ge_xSb_yTe_{1-x-y}$ phase diagram. The red and green lines correspond, respectively, to the stressed rigid and flexible phase. Blue circles represent the compositions studied by FPMD. The thick black line represents the rigidity transition line defined by Eq. (2) and separates the flexible (Te rich) from the stressed rigid phase where most PCMs can be found, especially on the $GeTe$-Sb_2Te_3 tie line (black line). Small green dots in the flexible phase represent bulk glass compositions obtained experimentally (Ref. 39).

estimate corresponding to $n_c=3$. Considering the numbers given in Table I, we make simple assumptions: Ge has four neighbors ($r_{Ge}=4$) with a fraction η_4 of tetrahedral sites, Sb has $r_{Sb}=3.8$ neighbors in a distorted octahedral geometry ($n_{Sb}^{BB}=3$), and Te has $r_{Te}=2.6$ neighbors and one BB constraint. Pure amorphous Ge is known to be a tetrahedral network and in $GeSb_6$ all Ge are tetrahedral ($\eta_4=1$, Figs. 6 and 12) and the addition of Te effectively lowers the fraction η_4 of tetrahedral Ge. For the sake of simplicity, we assume that $\eta_4=x+y$. Inserting these numbers into Eq. (2) and requesting $n_c=3$, one finally obtains a parameter-free rigidity transition line relating the compositions x and y,

$$y \approx \frac{7}{26+20x} - x. \tag{3}$$

The Maxwell line, defined by Eq. (3), is found to be close to the compositional join $GeTe_4$-$SbTe_4$ or, e.g., to the $GeSbTe_8$ alloy on the $Ge_xSb_xTe_{1-2x}$ tie line (Fig. 14). Equation (3) defines two regions in the GST triangle. In the tellurium-rich region the system has not enough Ge or Sb cross links to ensure rigidity and local deformations are allowed. In the second region, where usual PCMs are found, the amorphous phases are stressed rigid. Bulk glass formation seems to be only possible in the flexible phase as shown from experimental data.[39] This behavior clearly contrasts with sulfide and selenide analogs, and the origin of this difference in glass-forming ability will need additional studies to be fully understood. Undoubtedly, answers should be provided by a detailed study of the liquid phase, and we conjecture that the increase in the Te coordination number (thus in

the number of constraints) with temperature[40] is playing a key role, a feature that is not observed in sulfur and selenium liquids.

The location of the transition line in the compositional triangle (Fig. 14) appears also to be different from what is known in corresponding group IV-V selenides.[8] In the Ge-As-Se system where the 8-N rule holds, a Maxwell transition line is found along the As_2Se_3-$GeSe_4$ join as evidenced from isocoordination rule studies.[41] Compared to As_2Se_3, the shift of the transition to the chalcogen-rich compositions along the group V telluride axis can be understood from the present results. Since As has 4.5 constraints (1.5 BS and 3 BB) and Se has two constraints, whereas Sb has 4.85–4.9 constraints and Te has 2.15–2.20 constraints (Table I), the fulfillment of $n_c=3$ in tellurides will need less cross-linking (Sb) elements, and will therefore shift the transition line to the chalcogen-rich region.

Although the mechanical properties of the amorphous phase probably play a role in the recrystallization process, the most important direct application of the present analysis concerns the aging of the amorphous structure, and consequently the drift of its electrical resistivity with time. As aging has been found to be very small in optimally constrained glasses,[13] we expect small drifts for alloy compositions yielding a number of constraints close to the rigidity transition ($n_c=3$). Because of the need to have both an amorphous and a (meta)stable crystalline phase with the same global composition, not all the stoichiometries in the Ge-Sb-Te ternary can be considered for phase-change applications. However, doping an established PC material with elements contributing to a lowering of the constraints should lead to improved properties as far as the aging is concerned. This technologically important issue should obviously be addressed experimentally.

V. CONCLUSION

We have developed a constraint counting algorithm applicable to tellurides for which a simple counting based on the 8-N (octet) rule does not apply in a straightforward manner. We show that atomic scale trajectories obtained from first-principles molecular-dynamics simulations can be appropriately used for bond-stretching (BS) and bond-bending (BB) constraint counting and applied to the GST phase-change system, a family of huge technological interest. The results show that amorphous systems lying on the popular Sb_2Te_3-$GeTe$ tie line in the GST compositional triangle belong to a stressed rigid phase, whereas an isostatic stress-free Phillips-Thorpe rigidity transition line is obtained close to the $SbTe_4$-$GeTe_4$ join. We have sketched here the very general behavior and more detailed experimental and theoretical studies (e.g., along the $Ge_xSb_xTe_{1-2x}$ line shown in Fig. 14) close to the threshold are certainly welcome to fully characterize the transition. On the other hand, since it has been found in amorphous selenides and sulphides that compositions around this transition line display some remarkable properties such as absence of aging, stress-free character and space-filling tendencies,[9] one may wonder to what extent these properties can be observed in tellurides as well, and

how these properties, once being observed, could be used in close future to design phase-change materials with the corresponding functionality.

ACKNOWLEDGMENTS

[1] S. Ovshinsky, Phys. Rev. Lett. **21**, 1450 (1968).

[2] M. Wuttig and N. Yamada, Nature Mater. **6**, 824 (2007).

[3] *Phase Change Materials: Science And Applications*, edited by S. Raoux and M. Wuttig (Springer, New York, 2008).

[4] D. Lencer, M. Salinga, B. Grabowski, T. Hickel, J. Neugebauer, and M. Wuttig, Nature Mater. **7**, 972 (2008).

[5] H.-Y. Cheng, C. A. Jong, R.-J. Chung, T.-S. Chin, and R.-T. Huang, Semicond. Sci. Technol. **20**, 1111 (2005).

[6] A. V. Kolobov, P. Fons, A. I. Frenkel, A. L. Ankudinov, J. Tominaga, and T. Uruga, Nature Mater. **3**, 703 (2004).

[7] W. Welnic, A. Pamungkas, R. Detemple, C. Steimer, S. Blügel, and M. Wuttig, Nature Mater. **5**, 56 (2006).

[8] *Rigidity Theory and Applications*, edited by M. F. Thorpe and P. M. Duxbury (Kluwer Academic, Plenum Publishers, New York, 1999).

[9] *Rigidity and Boolchand Phases in Nanomaterials*, edited by M. Micoulaut and M. Popescu (INOE Publishing House, Bucarest, 2009).

[10] X. Feng, W. J. Bresser, and P. Boolchand, Phys. Rev. Lett. **78**, 4422 (1997).

[11] J. C. Phillips, J. Non-Cryst. Solids **34**, 153 (1979); M. F. Thorpe, *ibid.* **57**, 355 (1983).

[12] M. Micoulaut and J. C. Phillips, Phys. Rev. B **67**, 104204 (2003).

[13] S. Chakravarty, D. G. Georgiev, P. Boolchand, and M. Micoulaut, J. Phys.: Condens. Matter **17**, L1 (2005).

[14] M. Wuttig, D. Lüsebrink, D. Wamwangi, W. Welnic, M. Gillessen, and R. Dronkowski, Nature Mater. **6**, 122 (2007).

[15] C. Bichara, J. Y. Raty, and J.-P. Gaspard, Phys. Rev. B **53**, 206 (1996).

[16] J. Akola and R. O. Jones, Phys. Rev. B **76**, 235201 (2007).

[17] S. Caravati, M. Bernasconi, T. D. Kuehne, M. Krack, and M. Parrinello, Appl. Phys. Lett. **91**, 171906 (2007).

[18] C. Bichara, M. Johnson, and J.-P. Gaspard, Phys. Rev. B **75**, 060201(R) (2007).

[19] D. A. Baker, M. A. Paesler, G. Lucovsky, S. C. Agarwal, and P. C. Taylor, Phys. Rev. Lett. **96**, 255501 (2006).

[20] A. Feltz, H. Aust, and A. Blayer, J. Non-Cryst. Solids **55**, 179 (1983).

[21] M. Micoulaut, R. Vuilleumier, and C. Massobrio, Phys. Rev. B **79**, 214205 (2009).

[22] R. Car and M. Parrinello, Phys. Rev. Lett. **55**, 2471 (1985).

[23] A. D. Becke, Phys. Rev. A **38**, 3098 (1988); C. Lee, W. Yang, and R. G. Parr, Phys. Rev. B **37**, 785 (1988).

[24] W. G. Hoover, Phys. Rev. A **31**, 1695 (1985); S. Nosé, Mol. Phys. **52**, 255 (1984).

[25] G. Kresse and J. Hafner, Phys. Rev. B **47**, 558 (1993).

[26] P. E. Blöechl, C. J. Först, and J. Schimpl, Bull. Mater. Sci. **26**, 973 (2003).

[27] D. Vanderbilt, Phys. Rev. B **41**, 7892 (1990).

[28] J. P. Perdew and Y. Wang, Phys. Rev. B **45**, 13244 (1992).

[29] R. Shaltaf, E. Durgun, J.-Y. Raty, Ph. Ghosez, and X. Gonze, Phys. Rev. B **78**, 205203 (2008).

[30] J. C. Maxwell, Philos. Mag. **27**, 294 (1864).

[31] J. L. Lagrange, *Mécanique Analytique* (Paris, 1788).

[32] I. Petri, P. S. Salmon, and H. E. Fisher, Phys. Rev. Lett. **84**, 2413 (2000).

[33] B. Bureau, J. Troles, M. Le Floch, P. Guénot, F. Smektala, and J. Lucas, J. Non-Cryst. Solids **319**, 145 (2003).

[34] S. Kohara, K. Kato, S. Kimura, H. Tanaka, T. Usuki, K. Suzuya, H. Tanaka, Y. Moritomo, T. Matsunaga, N. Yamada, Y. Tanaka, H. Suematu, and M. Takata, Appl. Phys. Lett. **89**, 201910 (2006).

[35] Z. Sun, J. Zhou, and R. Ahuja, Phys. Rev. Lett. **98**, 055505 (2007); Z. Sun, J. Zhou, A. Blomqvist, B. Johansson, and R. Ahuja, *ibid.* **102**, 075504 (2009).

[36] Y. Maeda and M. Wakagi, Jpn. J. Appl. Phys. **30**, 101 (1991).

[37] J. Y. Raty, C. Otjacques, J. P. Gaspard, and C. Bichara, Solid State Sci. **12**, 193 (2010).

[38] D. Selvanathan, R. N. Enzweiler, W. J. Bresser, and P. Boolchand, Bull. Am. Phys. Soc. **42**, 249 (1997).

[39] P. Lebaudy, J. M. Saiter, J. Grenet, M. Belhadji, and C. Vautier, Mater. Sci. Eng., A **132**, 273 (1991).

[40] A. Menelle, R. Bellissent, and A. M. Flanck, EPL **4**, 705 (1987).

[41] W. A. Kamitakahara, R. L. Cappelletti, P. Boolchand, B. Halfpap, F. Gompf, D. A. Neumann, and H. Mutka, Phys. Rev. B **44**, 94 (1991).